SCIENCE CHINA
Information Sciences

• RESEARCH PAPER •

April 2025, Vol. 68, Iss. 4, 140402:1–140402:9
https://doi.org/10.1007/s11432-024-4046-x

Special Topic: Photonics Technology

High-temperature optoelectronic synaptic devices based on 4H-SiC

Mingxuan BU[1,2], Yue WANG[1,2], Zhenyi NI[1], Dongke LI[1,2*], Deren YANG[1,2] & Xiaodong PI[1,2*]

[1]*State Key Laboratory of Silicon and Advanced Semiconductor Materials & School of Materials Science and Engineering, Zhejiang University, Hangzhou 310027, China*
[2]*Institute of Advanced Semiconductors & Zhejiang Provincial Key Laboratory of Power Semiconductor Materials and Devices, ZJU-Hangzhou Global Scientific and Technological Innovation Center, Zhejiang University, Hangzhou 311200, China*

Received 6 April 2024/Revised 25 April 2024/Accepted 22 May 2024/Published online 26 February 2025

Abstract Optoelectronic synaptic devices operating at high temperatures have application potential across many important fields, including the aerospace and defense industries. However, limited research exists on such devices. Herein, we fabricate 4H-SiC-based high-temperature optoelectronic synaptic devices that are capable of achieving diverse synaptic functionalities at temperatures as high as 600 K. The synaptic functionalities are realized for these devices through carrier capture and release of the deep-level defects introduced via electronic irradiation. A 3 × 3 array of high-temperature optoelectronic synaptic devices enables the image memory functions. A neural network model constructed using this array addresses the issue of color quantization. The optoelectronic synaptic devices thus developed are capable of high-temperature applications.

Keywords optoelectronic synaptic devices, 4H-SiC, synaptic plasticity, neuromorphic computing, high-temperature devices

Citation Bu M X, Wang Y, Ni Z Y, et al. High-temperature optoelectronic synaptic devices based on 4H-SiC. Sci China Inf Sci, 2025, 68(4): 140402, https://doi.org/10.1007/s11432-024-4046-x

1 Introduction

Rapid advancements in artificial intelligence have led to a significant surge in the demand for computing power [1–3]. However, current computing systems based on the von Neumann architecture cause a bottleneck owing to the separate design requirement for memory and processing units, necessitating a trade-off between computing power and energy consumption [4–7]. The increasing requirements for high computing power, high processing speed, low power consumption, and low latency [8–10] have made it imperative to develop innovative computing systems. One particularly promising approach is the implementation of neuromorphic computing systems that mimic the architecture and functionalities of the human brain [11–16]. By incorporating optoelectronic integration into neuromorphic computing, researchers have envisioned that advantages such as high computing power, low energy consumption, low crosstalk, and large bandwidth may be realized [17–19].

Because optoelectronic synaptic devices are critical for neuromorphic computing based on optoelectronic integration, extensive research has been conducted on them. Currently, increasing efforts are being devoted to expending the use of optoelectronic synaptic devices in high-temperature environments [20–24]. However, optoelectronic synaptic devices based on two-dimensional materials, organic semiconductors, and semiconductor nanocrystals face challenges in overcoming their inherent limitations in terms of high-temperature stability [25–34]. Currently, high-temperature optoelectronic synaptic devices are primarily fabricated using wide-bandgap semiconductors [35–37], with the highest operating temperature reaching 473 K [20]. However, large-scale production of the materials (ScN, MoO_x, DPPDTT/MI, etc.) used in these studies [35–37] is challenging, hindering the scalability of the devices. As one of the most popular wide bandgap semiconductors, 4H-SiC possesses a bandgap of 3.26 eV and a high thermal conductivity of approximately 4 $W{\cdot}cm^{-1}{\cdot}K^{-1}$ [38]. Advanced crystal preparation and processing techniques applied to 4H-SiC have facilitated the extensive utilization of its devices under demanding conditions, including

* Corresponding author (email: ldkest@zju.edu.cn, xdpi@zju.edu.cn)

high-temperature, -voltage, and -power operational environments [39–44]. However, the use of 4H-SiC in high-temperature optoelectronic synaptic devices has not been previously demonstrated, despite a recent attempt [45, 46].

In this study, we fabricate 4H-SiC-based optoelectronic synaptic devices and demonstrate their applicability in high-temperature environments. A 4H-SiC wafer was first irradiated with high-energy electrons to generate high-concentration deep-level defects, which extended the lifetime of the photogenerated carriers in 4H-SiC. Owing to the wide bandgap of 4H-SiC and the long capture time of photogenerated carriers by the defects, the devices exhibited short- and long-term synaptic plasticity at both room temperature and temperatures up to 600 K. Additionally, we fabricated a 3×3 array of 4H-SiC synaptic devices to explore advanced applications in neural networks. The devices in this array showed good consistency, with a deviation in the operating currents below 10% at 600 K. An artificial neural network model that utilizes this array can effectively perform color quantization.

2 Experimental

Material preparation and device fabrication. A (0001) p-type 4H-SiC wafer with an aluminum concentration of 5×10^{17} cm^{-3} and a thickness of approximately 350 μm was used. First, the wafer was subjected to electron irradiation to generate defects. Electron irradiation was performed using a high-energy linear accelerator (CIAE-FZ-10/15; China Institute of Atomic Energy). During the irradiation, an electron beam with an energy of 10 MeV, power of 20 kW, and a dose of 100000 kGy was employed. After irradiation, the wafer was cleaned using the Radio Corporation of America (RCA) cleaning process. Subsequently, Al/Ti/Ni (100/50/50 nm) electrodes were fabricated on the wafer surface by sequentially sputtering Al, Ti, and Ni targets. Rapid thermal processing (at 600°C and 1000°C for 1 min in N_2 atmosphere) was subsequently carried out to form ohmic contacts between the Al/Ti/Ni electrodes and 4H-SiC. The size of the ohmic electrodes was 200×500 μm^2 with a lateral interval of 500 μm (Figure 1(a)). Finally, 100 nm Ti and 50 nm Au were deposited on the bottom of the 4H-SiC wafer and annealed at 550°C in N_2 for 3 min to form a global Schottky electrode.

Characterization. Deep-level transient spectroscopy (DLTS, Semilab, DLS-83D) was used to detect deep-level defects in the 4H-SiC wafer before and after irradiation. DLTS results (detailed in Figure S1) showed that defects induced by irradiation were primarily HK_4 [47, 48], with a high concentration of approximately 5×10^{16} cm^{-3}. The synaptic functionalities were characterized using a 405-nm wavelength laser (KYD405NX-X1240). Optical spikes were obtained using an optical shutter (SHM05/M, THORLABS) modulated by an electric pulse signal generator (AFG 31000 SERIES, Tektronix), and the optical power density was measured using a power meter (PM 100D, THORLABS). A semiconductor parameter analyzer (FS480, PRIMARIUS) and a source meter (Keithley 2636 B, Tektronix) were used to characterize the devices.

Color quantization simulation. The original image was a color image with dimensions of 1280×853 pixels. The competitive nodes in the competitive layer were associated with synaptic devices that reflect their characteristics. The RGB color information of each pixel in the original image was transformed into a three-dimensional vector and input into the competitive layer. Subsequently, the weight vectors were updated using the stochastic gradient descent (SGD) method, and the bubble function was chosen as the neighborhood function. Finally, the weight vectors were utilized as RGB color vectors to reconstruct the images.

3 Results and discussion

A schematic diagram of the developed 4H-SiC synaptic device is shown in Figure 1(a). The 4H-SiC wafer was optically active, and the photogenerated carriers acted as neurotransmitters. The 4H-SiC wafer used in this study underwent electron irradiation to generate high-concentration irradiation defects (detailed in Section 2) [47, 49]. As shown in Figure S2, the irradiation treatment extends the lifetime of the photogenerated carriers in the 4H-SiC device from a few microseconds to ∼2 s [50, 51], which is crucial for mimicking optically stimulated synaptic plasticity [52–54]. In addition, the in-gap states introduced by the defects [55] extend the photoresponse of 4H-SiC from the intrinsic excitation region (below 390 nm) to longer wavelengths (up to ∼700 nm) (Figure S3). To exploit the defect-induced states,

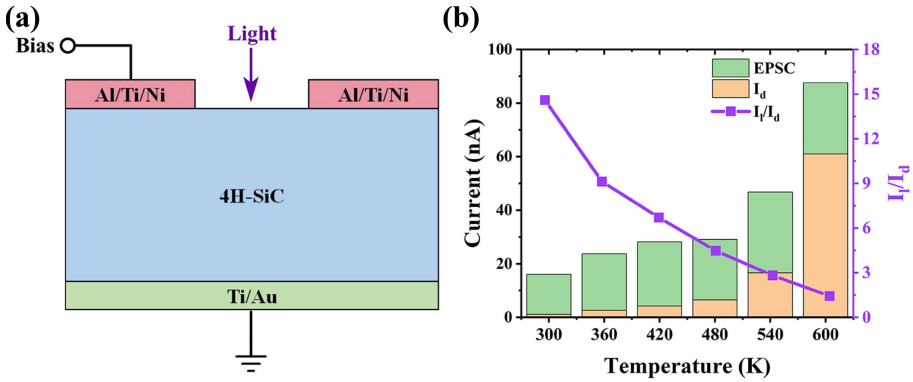

Figure 1 (Color online) (a) Schematic of the 4H-SiC synaptic device; (b) variations in EPSC, $I_{\rm d}$ and $I_{\rm l}/I_{\rm d}$ depending on the working temperature.

a representative excitation wavelength (405 nm) was used to stimulate the synaptic plasticity of the 4H-SiC synaptic device.

Asymmetric Al/Ti/Ni and Ti/Au electrodes were used in the 4H-SiC synaptic device, which served as the presynaptic and postsynaptic membranes, respectively. As shown in Figure S4, Ohmic and Schottky contacts are formed between Al/Ti/Ni and 4H-SiC and between Ti/Au and 4H-SiC, respectively. Such a device structure with asymmetric electrodes can effectively suppress dark currents, enabling large optical responsivity at high temperatures [56].

Figure 1(b) shows the variations in dark current ($I_{\rm d}$) and excitatory postsynaptic current (EPSC) with respect to the working temperature under optical stimulation. A bias voltage of -1.0 V was applied to the Al/Ti/Ni electrode during the test. The power density of light was 0.1 mW/cm^2, and the light pulse duration was 5.0 s. The $I_{\rm d}$ value was minimal at room temperature and gradually increased with the working temperature. However, the change in EPSC with increasing working temperature was not as significant as that in $I_{\rm d}$. The temperature-dependence of the light-to-dark current ratio ($I_{\rm l}/I_{\rm d}$) is shown in Figure 1(b); $I_{\rm l}$ represents the photocurrent, which is the sum of $I_{\rm d}$ and EPSC. At room temperature, the $I_{\rm l}/I_{\rm d}$ ratio was 14.6. With an increase in working temperature, the sensitivity of the device gradually decreased owing to an increase in $I_{\rm d}$. However, even at a high working temperature of 600 K, the $I_{\rm l}/I_{\rm d}$ ratio was maintained at approximately 1.43, indicating a clearer and more distinguishable high-temperature EPSC than those previously reported [35–37].

Figures 2(a)–(c) display the response of the 4H-SiC synaptic device to a single optical pulse at different temperatures. The bias voltage was -1.0 V, the optical power density was 0.1 mW/cm^2, and the pulse duration was 5.0 s. The photocurrent of the device initially increased rapidly and then gradually decreased upon the withdrawal of the optical excitation. Figure 2(g) depicts the spike-duration dependent plasticity (SDDP) at different temperatures. As the duration of the stimulation pulse increased, the EPSC initially increased and then reached saturation, resembling the behavior of biological synapses. Our results indicate that such SDDP occurs at all the temperatures between 300–600 K.

Paired pulse facilitation (PPF) plays a crucial role in the encoding and decoding of temporal information [57–64]. Figures 2(d)–(f) illustrate the PPF behaviors at 300, 480, and 600 K, respectively. A bias voltage of -1.0 V was applied to the top Al/Ti/Ni electrode. The duration of each optical pulse was 0.3 s, and the interval (Δt) between two pulses was 0.5 s. The device exhibited sharp and distinguishable EPSC peaks under stimulation by two pulses. The peak value of the EPSC generated by the second pulse was significantly higher than that generated by the first pulse. Figure 2(h) shows the PPF index (the ratio of the peak value of the EPSC generated by the second pulse to that generated by the first pulse) at different temperatures plotted against the interval between the two pulses. The data points represent the experimental measurement results, and the curves were fitted using a double-exponential function. It is evident that the PPF Index decreases with increasing temperature. This is because the photocurrent decays faster at higher temperatures. SDDP and PPF indicated that the optoelectronic synaptic device based on 4H-SiC exhibited good short-term plasticity (STP) at both room and high temperatures, possessing the potential to mimic the signal-transmission and information-encoding processes of biological synapses.

Long-term plasticity (LTP) was also studied. Figures 3(a)–(c) illustrate the spike-rate dependent plasticity (SRDP) at different temperatures. Ten optical pulses with the duration of 0.2 s and frequencies

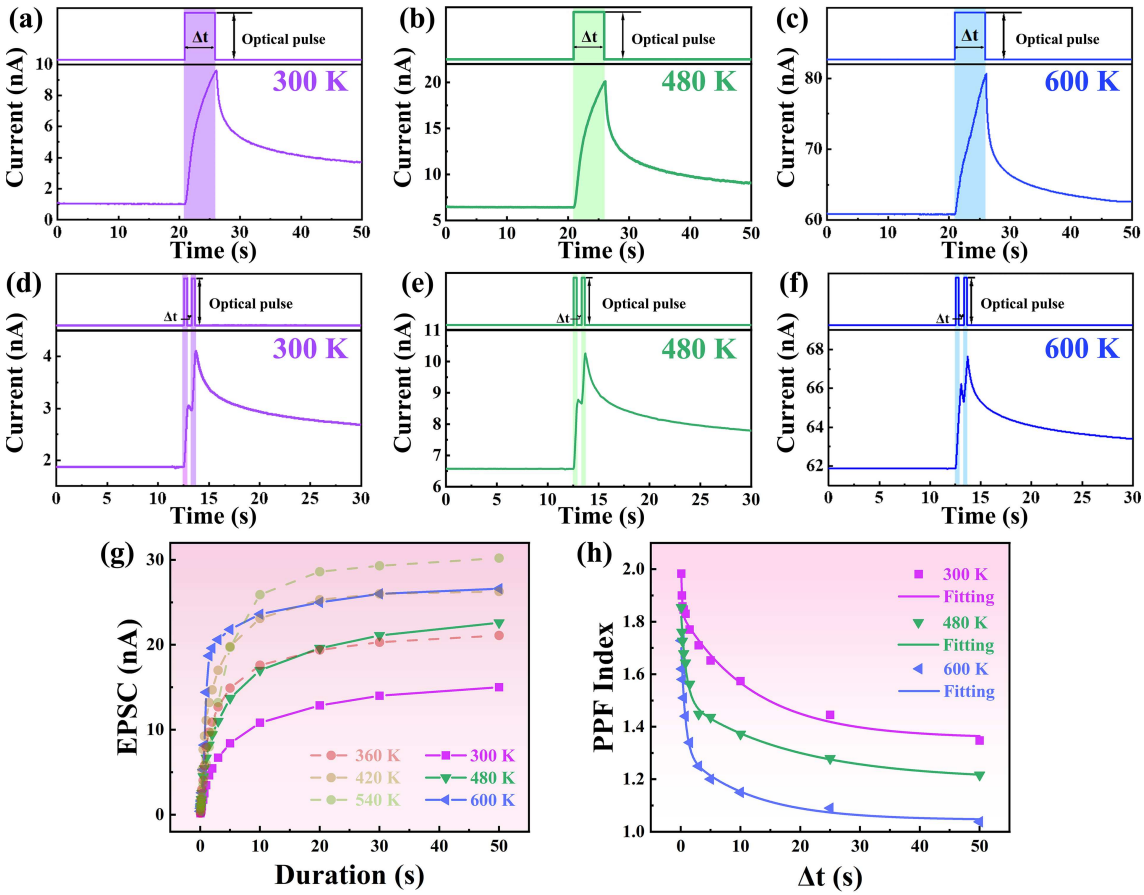

Figure 2 (Color online) Response at (a) 300 K, (b) 480 K, and (c) 600 K; PPF at (d) 300 K, (e) 480 K, and (f) 600 K; (g) SDDP under the stimulation of a single optical pulse; (h) dependence of the PPF index on Δt at different temperatures.

of 3.3, 1.0, and 0.5 Hz were used. Evidently, optical pulses at higher frequencies led to a higher peak value of the EPSC. Figures 3(d)–(f) show the spike-number dependent plasticity (SNDP) induced by the consecutive optical pulses with a duration of 0.2 s and an interval of 0.1 s. With an increase in the number of spikes, the EPSC initially increased and then exhibited a stable trend. This resembles the characteristics of the biological synapses.

The working process of the device is illustrated in Figure 4. During the operation, the device was reverse biased. As the optical excitation at 405 nm did not effectively generate intrinsic electron-hole pairs in 4H-SiC, the photoconductivity of the device is attributed primarily to the defects. Upon optical excitation, electrons at the defect levels of 4H-SiC absorb the energy of the photons and jump to the conduction band. The photogenerated electrons move towards the Schottky contact (Ti/Au), leading to a photocurrent. After removing the optical excitation, the photogenerated electrons in the conduction band may be recaptured by defects, allowing the device to return to its initial state. Therefore, the lifetime of the photocurrent of the device primarily depends on the trapping time of the photogenerated electrons at defects, which is mainly determined by the capture cross-section of defects for electrons as well as the energy gap between the defect levels and the conduction band [65]. The main defect in the current study was HK_4 (Figure S1). Although the exact value of the electron capture cross section of HK_4 could not be ascertained, the defect levels were up to 1.7 eV below the conduction band [47], enabling a long photocurrent lifetime.

Furthermore, a 3 × 3 array of 4H-SiC synaptic devices was fabricated to construct an artificial neural network. Figure S5 shows the three-dimensional stacked bar charts of the dark current and EPSC after 5 s of optical stimulation. The deviation between the devices (calculated by dividing the root mean square by the mean value) was only 9.07% at 600 K, demonstrating good uniformity in the device performance. The array was used to simulate the image learning and forgetting processes. The input image consisted of a 3 × 3 letter 'X' with the grayscale value of each pixel binarized and fed into the array of the synaptic devices. In Figure 5(a), the white square indicates that the device is not optically stimulated, while the

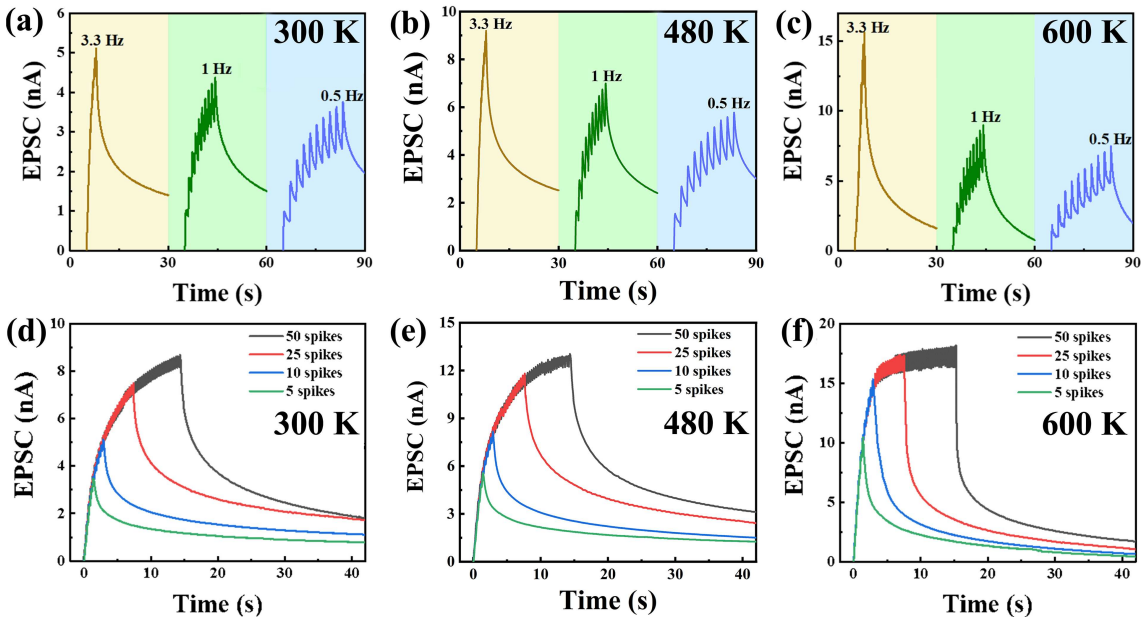

Figure 3 (Color online) SRDP at (a) 300 K, (b) 480 K, and (c) 600 K; SNDP at (d) 300 K, (e) 480 K, and (f) 600 K.

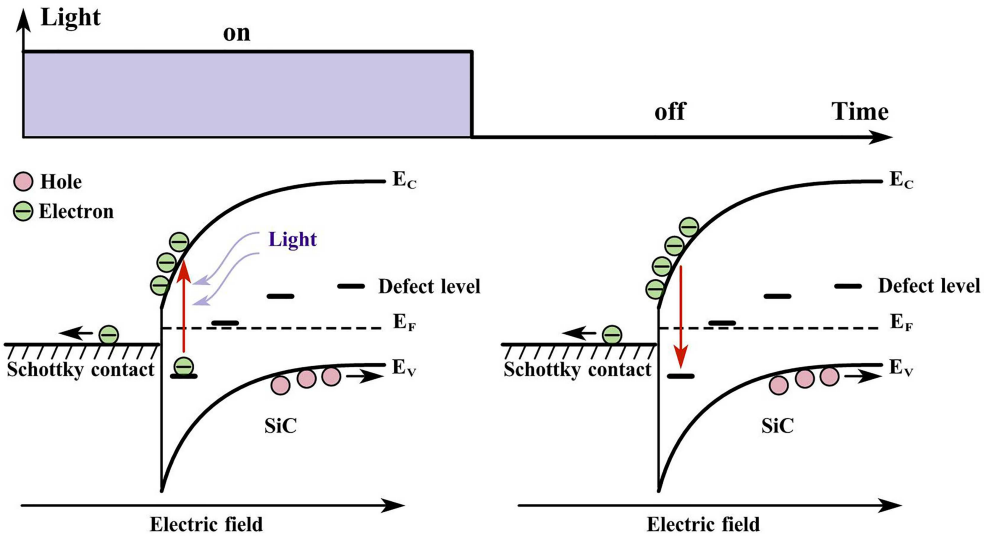

Figure 4 (Color online) Working process of the 4H-SiC device.

black square indicates that the device is optically stimulated by an optical pulse with a pulse width of 0.2 s. Each input is considered as one learning, and the array's memory effect for the input image is measured by its EPSC level. Figure 5(a) shows the memory status of the array after a single learning process and after continuous 10 learning processes at 600 K. Although there was a gradual decrease in the memory level after learning, the array managed to sustain commendable memory performance for an extended period. The memory effect can be measured as the sum of the EPSC for all devices in the array. Figure 5(b) shows the dependence of the memory effect on the number of spikes and elapsed time after learning; the total EPSC value after 10 optical pulses at 600 K is set to be '1'. It is evident that the array exhibited higher learning and forgetting rates at higher temperatures. As time increased, the memory effects at the different temperatures gradually became similar.

We constructed a self-organizing map (SOM) neural network to achieve color quantization, as shown in Figure 5(c). In each training epoch, the network learns from the input RGB color vectors and updates the weight vectors based on the learning rate. The learning rate of the network depends on the weight-change rate of the array. After learning, the image is reconstructed based on the trained weight vectors. The quantization error, which was measured by averaging the Euclidean distance between each

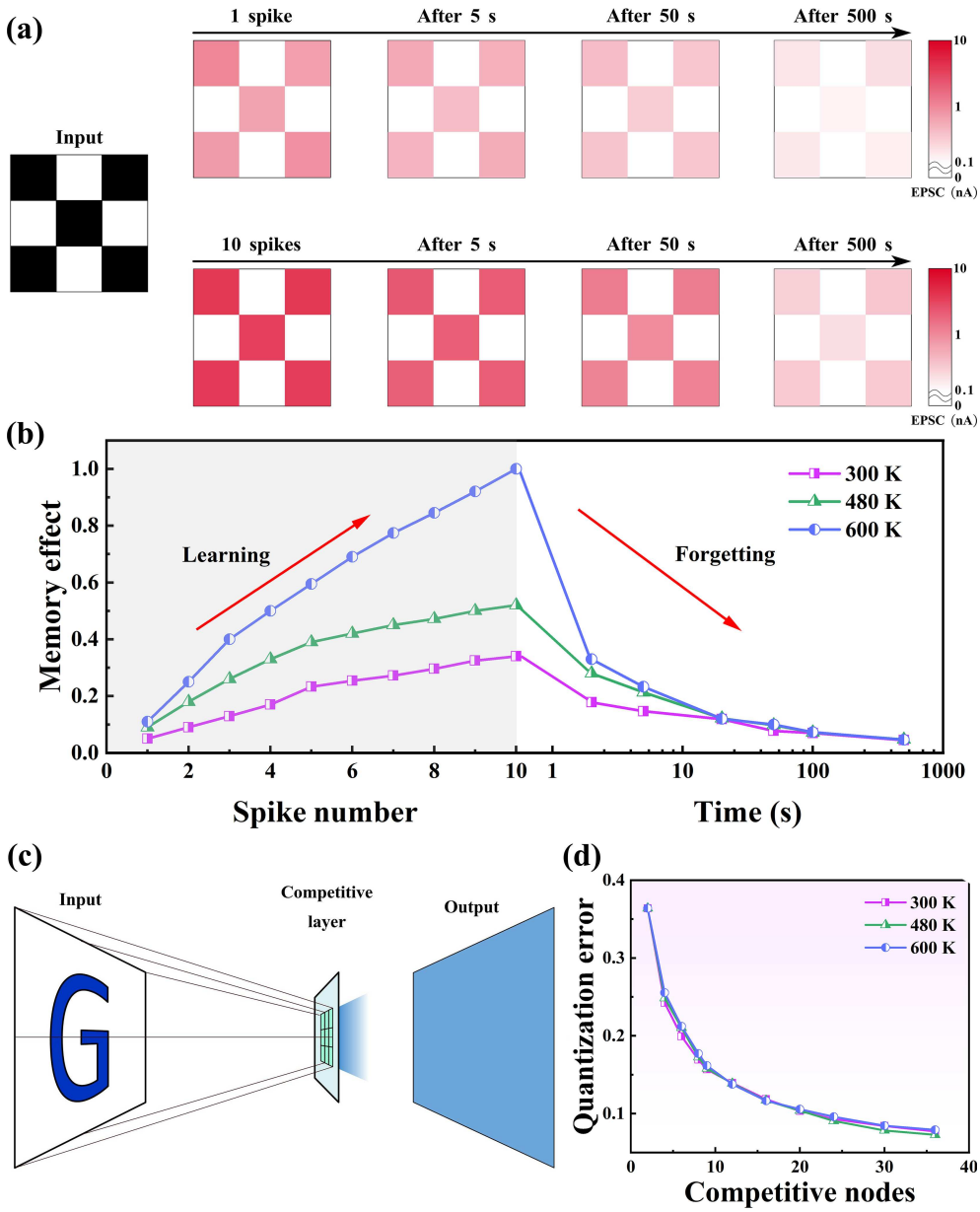

Figure 5 (Color online) (a) Memory effect on images after a single learning process and 10 continuous learning processes at 600 K; (b) the learning and forgetting process of the array at different temperatures; (c) schematic of the array-based SOM neural network; (d) dependence of the quantization error on the number of competitive nodes.

input color vector and the trained weight vector of the nearest competing node, was used to evaluate the result. A smaller quantization error indicates less loss in image quality after quantization, and therefore, a better quantization result. Figure 5(d) displays the measured quantization errors related to the number of nodes in the competitive layer. Each quantization error value was calculated as the average of 100 runs, with each run containing 50 training epochs. The quantization error steadily decreased as the number of competing nodes increased. Significantly, the quantization error of the network is essentially independent of the temperature, indicating the stability of the color quantization capability of the array at different temperatures. This was probably because the difference in the rate of weight change at different temperatures was not significant, as shown in Figures 3(d)–(f). The visual processing results for the SOM network are shown in Figure S6. For the six-competing-nodes processing, the quality of the quantized images was noticeably lower than that of the input. Only the primary elements of the input images were identified. When the number of competing nodes increased to 12, the image quality improved significantly. However, there were still noticeable differences compared with the original image. During the processing of the network with 24 competing nodes, the output images closely approximated the input.

Through the utilization of an array-based SOM network, the color space of a colored image was compressed from approximately 16000000 to 24, resulting in significant data compression while maintaining acceptable image quality. This result presents a promising avenue for the application of neuromorphic computing to visual processing systems based on optoelectronic synaptic devices.

Additionally, the 4H-SiC synaptic device exhibited high sensitivity to light. As shown in Figure S7, the device presents a clear response to an optical pulse with the power density as low as 6 $\mu W \cdot cm^{-2}$ (405 nm) at 600 K. Table S1 provides a summary of the reported high-temperature optoelectronic synaptic devices. To highlight the properties of the device at high temperatures, we focused on the maximum operating temperature. It is noteworthy that the operating temperature of the 4H-SiC optoelectronic synaptic device in this study was higher than those of similar devices reported to date. This suggests that optoelectronic synaptic devices based on 4H-SiC hold promise in meeting the elevated-temperature demands.

4 Conclusion

We fabricated high-temperature optoelectronic synaptic devices based on 4H-SiC, and achieved various synaptic functions at temperatures as high as 600 K. The 4H-SiC devices were used for artificial neural networks with optical stimulation. When faced with the color quantization problem, the neural network model based on a 3×3 array of 4H-SiC synaptic devices exhibited a stable processing effect at different temperatures. The devices demonstrated in this study present application potential as high-temperature optoelectronic synaptic devices that expand the operating temperature range of optoelectronic neuromorphic computing systems. This study provides valuable insights into applications relevant to computer vision and offers a viable approach for addressing image-related challenges under high-temperature conditions.

Acknowledgements This work was supported by National Natural Science Foundation of China (Grant Nos. U22A2075, 92364204, 91964107, U20A20209), Fundamental Research Funds for the Central Universities (Grant No. 226-2022-00200), and Leading Innovative and Entrepreneur Team Introduction Program of Hangzhou (Grant No. TD2022012). Dr. Pi acknowledges support from the Qianjiang Distinguished Expert Program in Hangzhou.

Supporting information Table S1 and Figures S1–S7. The supporting information is available online at info.scichina.com and link.springer.com. The supporting materials are published as submitted, without typesetting or editing. The responsibility for scientific accuracy and content remains entirely with the authors.

References

1 Wang Q, Mi N, Yi Z N, et al. Access data analysis technology and implementation of electric power big data achievement sharing platform through artificial intelligence. J Phys-Conf Ser, 2021, 2083: 032065
2 Hu Y C, Lin Y H, Lin C H. Artificial intelligence, accelerated in parallel computing and applied to nonintrusive appliance load monitoring for residential demand-side management in a smart grid: a comparative study. Appl Sci, 2020, 10: 8114
3 Wen W, Guo Y L, Liu Y Q. Multifunctional neurosynaptic devices for human perception systems. J Semicond, 2022, 43: 051201
4 Brodowicz M, Sterling T. A non von Neumann continuum computer architecture for scalability beyond Moore's law. In: Proceedings of the ACM International Conference on Computing Frontiers, 2016. 335–338
5 Mo P H, Li C, Zhao D, et al. Accurate and efficient molecular dynamics based on machine learning and non von Neumann architecture. npj Comput Mater, 2022, 8: 107
6 Shaafiee M, Logeswaran R, Seddon A. Overcoming the limitations of von Neumann architecture in big data systems. In: Proceedings of the 7th International Conference on Cloud Computing, Data Science & Engineering-Confluence, Noida, 2017. 199–203
7 He L C, Li X, Xie C C, et al. In-memory computing based on phase change memory for high energy efficiency. Sci China Inf Sci, 2023, 66: 200402
8 Wu J, Zhou P, Chen Q M, et al. Blockchain-based privacy-aware contextual online learning for collaborative edge-cloud-enabled nursing system in Internet of Things. IEEE Internet Things J, 2023, 10: 6703–6717
9 Gallego G, Delbruck T, Orchard G, et al. Event-based vision: a survey. IEEE Trans Pattern Anal Mach Intell, 2022, 44: 154–180
10 Akhoon M S, Suandi S A, Alshahrani A, et al. High performance accelerators for deep neural networks: a review. Expert Syst, 2022, 39: e12831
11 Kumar S, Wang X, Strachan J P, et al. Dynamical memristors for higher-complexity neuromorphic computing. Nat Rev Mater, 2022, 7: 575–591
12 Marković D, Mizrahi A, Querlioz D, et al. Author correction: physics for neuromorphic computing. Nat Rev Phys, 2021, 3: 671
13 Shastri B J, Tait A N, de Lima T F, et al. Photonics for artificial intelligence and neuromorphic computing. Nat Photonics, 2021, 15: 102–114
14 Park J Y, Choe D H, Lee D H, et al. Revival of ferroelectric memories based on emerging fluorite-structured ferroelectrics. Adv Mater, 2023, 35: 2204904
15 Wang Y, Yin L, Huang W, et al. Optoelectronic synaptic devices for neuromorphic computing. Adv Intell Syst, 2021, 3: 2000099
16 Mikolajick T, Park M H, Begon-Lours L, et al. From ferroelectric material optimization to neuromorphic devices. Adv Mater, 2023, 35: 2206042

17 Du W, Li C H, Huang Y X, et al. An optoelectronic reservoir computing for temporal information processing. IEEE Electron Device Lett, 2022, 43: 406–409
18 Li Y, Xuan Z, Lu J, et al. One transistor one electrolyte-gated transistor based spiking neural network for power-efficient neuromorphic computing system. Adv Funct Mater, 2021, 31: 2100042
19 Ni Y, Yang L, Feng J, et al. Flexible optoelectronic neural transistors with broadband spectrum sensing and instant electrical processing for multimodal neuromorphic computing. SmartMat, 2023, 4: e1154
20 Kai C H, Wang Y, Liu X, et al. AlGaN/GaN-based optoelectronic synaptic devices for neuromorphic computing. Adv Opt Mater, 2023, 11: 2202105
21 Chen G X, Yu X P, Gao C S, et al. Temperature-controlled multisensory neuromorphic devices for artificial visual dynamic capture enhancement. Nano Res, 2023, 16: 7661–7670
22 Mehregany M, Zorman C A, Rajan N, et al. Silicon carbide MEMS for harsh environments. Proc IEEE, 1998, 86: 1594–1609
23 Werner M R, Fahrner W R. Review on materials, microsensors, systems and devices for high-temperature and harsh-environment applications. IEEE Trans Ind Electron, 2001, 48: 249–257
24 Zhang H C, Sun Y, Hu K P, et al. Boosted high-temperature electrical characteristics of AlGaN/GaN HEMTs with rationally designed compositionally graded AlGaN back barriers. Sci China Inf Sci, 2023, 66: 182405
25 Lu Z J, Zhu M J, Liu Y F, et al. Low-temperature synthesis of boron nitride as a large-scale passivation and protection layer for two-dimensional materials and high-performance devices. ACS Appl Mater Inter, 2022, 14: 25984–25992
26 Mussa Y, Fathima A, Arsalan M, et al. The use of two-dimensional materials in high-temperature rechargeable batteries: current issues and preventative measures. Mater Res Express, 2019, 6: 092003
27 Shangguan W, Yan C X, Li W Q, et al. Two-dimensional semiconductor materials with high stability and electron mobility in group-11 chalcogenide compounds: MNX (M = Cu, Ag, Au; N = Cu, Ag, Au; X = S, Se, Te; M ≠ N). Nanoscale, 2022, 14: 4271–4280
28 Zhou F, Liu Y, Kuang M, et al. Time-reversal-breaking Weyl nodal lines in two-dimensional A_3C_2 (A = Ti, Zr, and Hf) intrinsically ferromagnetic materials with high Curie temperature. Nanoscale, 2021, 13: 8235–8241
29 Li Y Y, Wang Y, Yin L, et al. Silicon-based inorganic-organic hybrid optoelectronic synaptic devices simulating cross-modal learning. Sci China Inf Sci, 2021, 64: 162401
30 Wang Y, Yin L, Huang S J, et al. Silicon-nanomembrane-based broadband synaptic phototransistors for neuromorphic vision. Nano Lett, 2023, 23: 8460–8467
31 Chen Z, Li J F, Li T Z, et al. A CRISPR/Cas12a-empowered surface plasmon resonance platform for rapid and specific diagnosis of the Omicron variant of SARS-CoV-2. Natl Sci Rev, 2022, 9: nwac104
32 Zheng F, Chen Z, Li J F, et al. A highly sensitive CRISPR-empowered surface plasmon resonance sensor for diagnosis of inherited diseases with femtomolar-level real-time quantification. Adv Sci, 2022, 9: e2105231
33 Cui Y Y, Tong Z Y, Zhang X L, et al. Mid-infrared plasmonic silicon quantum dot/HgCdTe photodetector with ultrahigh specific detectivity. Sci China Inf Sci, 2023, 66: 142404
34 Huang W, Xia X W, Zhang H X, et al. High-performance carbon-electrode-based self-powered optoelectronic synaptic devices. Sci China Inf Sci, 2024, 67: 159403
35 Rao D, Pillai A I K, Garbrecht M, et al. Scandium nitride as a gateway III-nitride semiconductor for both excitatory and inhibitory optoelectronic artificial synaptic devices. Adv Elect Mater, 2023, 9: 2200975
36 Guo Z Y, Zhang J Y, Yang B, et al. Organic high-temperature synaptic phototransistors for energy-efficient neuromorphic computing. Adv Mater, 2024, 36: 2310155
37 Zhao J S, Zheng S T, Zhou L W, et al. An artificial optoelectronic synapse based on MoO_x film. Nanotechnology, 2023, 34: 145201
38 Kimoto T, Cooper J A. Fundamentals of Silicon Carbide Technology: Growth, Characterization, Devices and Applications. Newark: Wiley, 2014. 189–276
39 Hung C L, Cheng J C, Tsui B Y. Failure analysis on TiAl metallization process for ohmic contact on 4H-SiC pMOSFET. In: Proceedings of IEEE 26th International Symposium on Physical and Failure Analysis of Integrated Circuits (IPFA), Hangzhou, 2019. 8984917
40 Wang Z M, Liu L. Simulation research of 4H-SiC double-trench MOSFET with high-k gate dielectric materials. In: Proceedings of International Workshop on Advanced Patterning Solutions (IWAPS), Foshan, 2021. 1–4
41 Sciuto A, Torrisi L, Cannavó A, et al. Advantages and limits of 4H-SiC detectors for high- and low-flux radiations. J Elec Materi, 2017, 46: 6403–6410
42 Meyer D J, Downey B P, Katzer D S, et al. Epitaxial lift-off and transfer of III-N materials and devices from SiC substrates. IEEE Trans Semicond Manufact, 2016, 29: 384–389
43 Wang W T, Lu X S, Wu X K, et al. Chemical-mechanical polishing of 4H silicon carbide wafers. Adv Mater Inter, 2023, 10: 2202369
44 Geng W H, Yang G, Zhang X Q, et al. Identification of subsurface damage of 4H-SiC wafers by combining photo-chemical etching and molten-alkali etching. J Semicond, 2022, 43: 102801
45 Liu X, Huang W, Kai C H, et al. Photogated synaptic transistors based on the heterostructure of 4H-SiC and organic semiconductors for neuromorphic ultraviolet vision. ACS Appl Electron Mater, 2023, 5: 367–374
46 Seo J H. Editorial for the special issue on wide bandgap semiconductor based micro/nano devices. Micromachines, 2019, 10: 213
47 Alfieri G, Kimoto T. Minority carrier transient spectroscopy of as-grown, electron irradiated and thermally oxidized p-type 4H-SiC. Mater Sci Forum, 2014, 778-780: 269–272
48 Kawahara K, Alfieri G, Hiyoshi T, et al. Effects of thermal oxidation on deep levels generated by ion implantation into n-type and p-type 4H-SiC. Mater Sci Forum, 2010, 645-648: 651–654
49 Reshanov S A, Beljakowa S, Zippelius B, et al. Thermal stability of defect centers in n- and p-type 4H-SiC epilayers generated by irradiation with high-energy electrons. Mater Sci Forum, 2010, 645-648: 423–426
50 Tan H, Ni Z Y, Peng W B, et al. Broadband optoelectronic synaptic devices based on silicon nanocrystals for neuromorphic computing. Nano Energy, 2018, 52: 422–430
51 Li H K, Chen T P, Liu P, et al. A light-stimulated synaptic transistor with synaptic plasticity and memory functions based on $InGaZnO_x$-Al_2O_3 thin film structure. J Appl Phys, 2016, 119: 244505
52 Kim K, Lim J G, Hu S M, et al. Multifilamentary switching of Cu/SiO_x memristive devices with a Ge-implanted a-Si underlayer for analog synaptic devices. NPG Asia Mater, 2023, 15: 48
53 Kim T S, Jeon S H, Ko K, et al. Fast, Energy-efficient InGaAs synaptic phototransistors on flexible substrate. Adv Elect Mater, 2023, 9: 2300437
54 Lei P X, Duan H, Qin L, et al. High-performance memristor based on 2D layered BiOI nanosheet for low-power artificial optoelectronic synapses. Adv Funct Mater, 2022, 32: 2201276
55 Åberg D, Hallén A, Svensson B G. Low-dose ion implanted epitaxial 4H-SiC investigated by deep level transient spectroscopy. Physica B-Condensed Matter, 1999, 273–274: 672–676
56 Mandal K C, Kleppinger J W, Chaudhuri S K. Advances in high-resolution radiation detection using 4H-SiC epitaxial layer devices. Micromachines, 2020, 11: 254

57 Wang J B, Li Y X, Zhang Y, et al. A two-terminal electric-double-layer synaptic device with short-term plasticity. In: Proceedings of IEEE 2nd Electron Devices Technology and Manufacturing Conference (EDTM), Kobe, 2018. 157–159
58 Seo Y T, Lee M S, Kim C H, et al. Si-based FET-type synaptic device with short-term and long-term plasticity using high-k gate-stack. IEEE Trans Electron Dev, 2019, 66: 917–923
59 Isope P. Short-term synaptic plasticity and the 'active calcium' hypothesis at a central synapse. J Physiol, 2013, 591: 4681–4682
60 Awiszus F, Feistner H, Urbach D, et al. Characterisation of paired-pulse transcranial magnetic stimulation conditions yielding intracortical inhibition or I-wave facilitation using a threshold-hunting paradigm. Exp Brain Res, 1999, 129: 317–324
61 Müller M, Felmy F, Schwaller B, et al. Parvalbumin is a mobile presynaptic Ca^{2+} buffer in the calyx of held that accelerates the decay of Ca^{2+} and short-term facilitation. J Neurosci, 2007, 27: 2261–2271
62 Tanim M M H, Templin Z, Hood K, et al. A natural organic artificial synaptic device made from a honey and carbon nanotube admixture for neuromorphic computing. Adv Mater Technol, 2023, 8: 2202194
63 Walters B, Jacob M V, Amirsoleimani A, et al. A review of graphene-based memristive neuromorphic devices and circuits. Adv Intell Syst, 2023, 5: 2300136
64 Zhu L Q, Wan C J, Guo L Q, et al. Artificial synapse network on inorganic proton conductor for neuromorphic systems. Nat Commun, 2014, 5: 3158
65 Shockley W, Read W T. Statistics of the recombinations of holes and electrons. Phys Rev, 1952, 87: 835–842